mater.scichina.com link.springer.com https://doi.org/10.1007/s40843-024-3239-y

g-C_3N_4 modified MoS_2 photoelectrodes for stable photo-assisted zinc-ion capacitors

Changhua Mi, Xin Sun, Xiaojing Yin, Jiahao Yang, Yanlong Lv, Xiaojun Lv and Meicheng Li*

ABSTRACT Photo-assisted capacitors are attractive devices for solar energy conversion and storage, while the behavior of photoelectrodes limits their performance. In this work, MoS_2 photoelectrodes were modified by g-C_3N_4, exhibiting enhanced photo-rechargeable properties. Our results show that the introduction of g-C_3N_4 increases the surface area of MoS_2 photoelectrodes and promotes the transport of charge carriers, which can boost the specific capacity and cycle stability of capacitors. The as-prepared zinc-ion capacitors with g-C_3N_4/MoS_2 photoelectrodes show a specific capacity of 380.93 F/g at 1 A/g under AM 1.5 G illumination. Remarkably, after 3000 cycles at 10 A/g, the capacity of the photo-assisted zinc-ion capacitor retains above 99%.

Keywords: g-C_3N_4/MoS_2 heterojunction, photo-assisted capacitor, zinc-ion capacitor, photogenerated carriers, photoelectrode

INTRODUCTION

Increasing the use of clean energy is a crucial strategy for enhancing sustainable energy development. Solar energy has garnered significant social attention due to its abundant resources, environmental friendliness, and vast potential for development and application [1,2]. However, the intermittent and fluctuating nature of solar energy presents significant challenges in maintaining the balance of grid demand [3,4]. Photo-rechargeable or photo-assisted charging energy storage devices enable the simultaneous conversion and storage of solar energy, effectively addressing the aforementioned challenges [5,6]. These devices typically utilize semiconductor materials as dual-function electrodes, integrating both photoelectric conversion and energy storage capabilities [7,8]. When illuminated, the photoelectrode generates electron-hole pairs that contribute to the charge-discharge process of the energy storage device, thereby achieving photo-assisted energy storage [8]. In recent years, numerous academic pioneers have conducted extensive research on photo-assisted energy storage devices. These devices, which include metal-ion batteries [9–11], capacitors [12–14], flow batteries [3,15], and metal-air batteries [16,17], are capable of being charged by solar energy, thereby reducing electrical energy consumption. However, photoelectrodes encounter significant challenges under illumination, including severe recombination of electron-hole pairs and structural degradation, which reduce both photocharging efficiency and stability [18]. Therefore, the development of appropriate photoelectrode materials is essential for optimizing photo-assisted energy storage devices.

In recent years, transition metal sulfides, particularly 2H-type MoS_2, have garnered significant attention for their applications in solar energy conversion and storage [19–21]. MoS_2 is a representative few-layer layered semiconductor that exhibits a tunable bandgap and a broad range of visible light absorption [20,22]. The proper positioning of the conduction band allows for the efficient transport of photogenerated electrons to the conductive substrate of the photoelectrode, thereby facilitating effective photoelectrical conversion [23,24]. The incorporation of a molybdenum metal layer between two sulfur layers, combined with the relatively weak van der Waals interactions of the layers, facilitates the intercalation and de-intercalation of metal ions [25]. This has successfully integrated MoS_2 materials into the emerging field of photocharging energy storage, with preliminary investigations into their dual-function capabilities [26]. One-dimensional ordered MoS_2 nanotubes can effectively inhibit the recombination of photogenerated electron-hole pairs, enabling a greater number of photogenerated carriers to engage in energy storage reactions [17]. This advancement has resulted in the highest reported kinetics for oxygen reduction reactions in photo-assisted zinc-air batteries. Boruah *et al.* [27] reported the direct growth of MoS_2 on ZnO-coated carbon felts, enabling the photocharging zinc-ion batteries to achieve approximately 1.8% photo-conversion efficiency under a 455 nm light source. However, the limited conductivity of MoS_2 and its propensity for lamellar aggregation hinder its application in the field of photocharging energy storage [20]. Researchers often combine MoS_2 with other materials, which can significantly improve the overall performance of the composite [28,29]. g-C_3N_4 materials possess inherent advantages, including excellent chemical stability, an appropriate bandgap, and low cost, which have led to their initial applications in the field of photo-assisted energy storage [30,31]. Moreover, the formation of heterojunctions between g-C_3N_4 and MoS_2 significantly enhances the separation efficiency of photogenerated charge carriers due to the influence of the built-in electric field [32]. Therefore, g-C_3N_4/MoS_2 materials hold significant potential for application in photo-assisted energy storage devices.

We present a photo-assisted rechargeable zinc-ion capacitor (PA-ZIC) that utilizes a g-C_3N_4/MoS_2 electrode. The g-C_3N_4/MoS_2 materials were synthesized through a two-step *in situ* growth process [32,33]. The incorporation of porous g-C_3N_4 powder increases the surface area of the composite. Further-

State Key Laboratory of Alternate Electrical Power System with Renewable Energy Sources, School of New Energy, North China Electric Power University, Beijing 102206, China
* Corresponding author (email: mcli@ncepu.edu.cn)

more, the synthesized g-C_3N_4 and MoS_2 exhibit well-matched band positions, facilitating the formation of a type II heterojunction that enhances the transport of photogenerated charge carriers. In the external circuit, the migration of photogenerated electrons aligns with the direction of electron flow within the zinc-ion capacitor. As a result, the photo-assisted energy storage performance is significantly enhanced. Compared to the specific capacitance of 334.35 F/g under dark conditions, the specific capacitance increases to 380.93 F/g at 1 A/g, showing an improvement of 13.93% under light. The PA-ZIC operates reliably for 3000 cycles, maintaining over 99% of its initial specific capacitance. This performance demonstrates a significant advantage over other capacitors. The structural design approach of g-C_3N_4/MoS_2 electrode materials is an attractive method for enhancing photo-assisted energy storage capabilities.

EXPERIMENTAL SECTION

Synthesis of g-C_3N_4/MoS_2

Urea (10 g) was weighed and placed into a crucible. It was heated at 60°C for 3 h and then transferred to a muffle furnace at 550°C for an additional 3 h [30,32]. After that, the yellow bulk powder was identified as g-C_3N_4. The bulk g-C_3N_4 was finely ground into a powder, and 50, 150, and 250 mg of the g-C_3N_4 powder were individually placed into separate 50 mL beakers. g-C_3N_4 was subjected to ultrasonic treatment with a suitable amount of deionized water for 6 h. Then, 1.21 g of sodium molybdate dihydrate and 2.275 g of thiourea were added to the solution. After the above solution was completely dissolved, it was transferred to 50 mL polytetrafluoroethylene reactors. The hydrothermal process was carried out by heating at 200°C for 24 h. The obtained suspension was removed after the reactor cooled down and then centrifuged several times with ethanol and deionized water to separate the black solid product [32,33]. The resulting black product was thoroughly dehydrated after vacuum drying at 60°C for 12 h. g-C_3N_4/MoS_2 products with varying g-C_3N_4 contents were prepared through careful grinding. The three samples were labeled g-C_3N_4/MoS_2-50, g-C_3N_4/MoS_2-150, and g-C_3N_4/MoS_2-250. The pure MoS_2 material was synthesized using the hydrothermal method described previously, without the addition of g-C_3N_4 suspension.

Preparation of photoelectrode

First, 5 mg of polyvinylidene fluoride (PVDF) adhesive was added to a suitable amount of *N*-methyl-2-pyrrolidone (NMP). The mixture was then subjected to ultrasonic treatment, agitation, and stirring until the PVDF was completely dissolved. Then, 5 mg of reduced graphene oxide (r-GO) was added as a conductive agent to the solution and stirred thoroughly. To synthesize the electrode solution, 90 mg of g-C_3N_4/MoS_2 was added and stirred for 12 h. At the same time, the indium tin oxide (ITO) conductive glass substrate underwent three sequential ultrasonic cleaning cycles using alcohol and deionized water, followed by thorough drying. Subsequently, a photocathode was fabricated on the ITO surface using the spin-coating technique. Before the spin-coating process, high-temperature-resistant tape was meticulously applied to designated areas of the ITO substrate to ensure precise coverage and protection during the coating procedure. The suspension was then evenly deposited onto the ITO glass surface, followed by vacuum-drying at 60°C for 12 h to facilitate solvent evaporation and promote uniform film formation. Upon completion of the drying process, the tape was carefully removed, resulting in the successful fabrication of the photoelectrode.

Fabrication of PA-ZIC

The CR2032 coin cell of type PA-ZIC features a 10 mm diameter hole at the center of the positive electrode casing. The glass-based cathode electrode was axially aligned and affixed to the positive shell, serving as an optical window. To prevent electrolyte leakage, epoxy resin was applied to seal the gap between the glass electrode and the positive casing. Conductive tape was utilized to create an electrical pathway, ensuring a secure connection between the photocathode and the positive shell. A 16 mm diameter Whatman glass microfiber filter was placed onto the photoelectrode, and approximately 150 μL of 3 M $Zn(CF_3SO_3)_2$ aqueous electrolyte was evenly applied over it. A zinc sheet was then positioned on the Whatman glass microfiber filter to function as the counter electrode. The gasket, shrapnel, and negative shell were sequentially assembled to construct the optical coin capacitor following the standard procedure.

Material characterization

The morphology of the samples was examined using scanning electron microscopy (SEM, TESCAN MIRA LMS) and transmission electron microscopy (TEM, JEOL JEM-F200). The crystallinity of the samples was assessed using an X-ray diffractometer (XRD, Bruker D8 Advance). The material composition was analyzed by scanning various elements with an X-ray photoelectron spectrometer (XPS, Thermo Scientific K-Alpha). The Brunauer-Emmett-Teller (BET) method was employed to determine the specific surface area and pore size of different materials in a nitrogen (N_2) environment.

Electrochemical test

The photosensitivity properties of the samples were evaluated using a three-electrode system within a 50 mm × 50 mm square electrolytic cell. At room temperature, the tests were conducted with an electrochemical workstation. Specifically, the photoresponse experiment was performed in a 2 M $ZnSO_4$ electrolyte. ITO glass with an effective area of 10 mm × 10 mm was used as the working electrode collector. A platinum plate was utilized as the counter electrode, while an Ag/AgCl electrode served as the reference electrode. A xenon lamp acted as the light source in this study.

Cyclic voltammetry (CV) testing of zinc-ion capacitors was conducted using an electrochemical workstation, with scan rates ranging from 5 to 100 mV/s within a voltage window of 0.2 to 1 V. Galvanostatic charge-discharge (GCD) tests were performed using Land testing system equipment, with current densities ranging from 0.5 to 10 A/g within the same voltage window of 0.2 to 1 V. The test parameters were consistently maintained under both light and dark conditions. The frequency for electrochemical impedance spectroscopy (EIS) testing of the zinc-ion capacitor ranged from 10 mHz to 100 kHz, with a voltage amplitude of 5 mV.

RESULTS AND DISCUSSION

Fig. 1a displays the XRD patterns of g-C_3N_4, MoS_2, and g-C_3N_4/MoS_2. The black line indicates that g-C_3N_4 exhibits two distinct diffraction peaks at 13.4° and 27.5°, as marked by the diamond symbol. The prominent peak at 27.5° can be labeled as the (002)

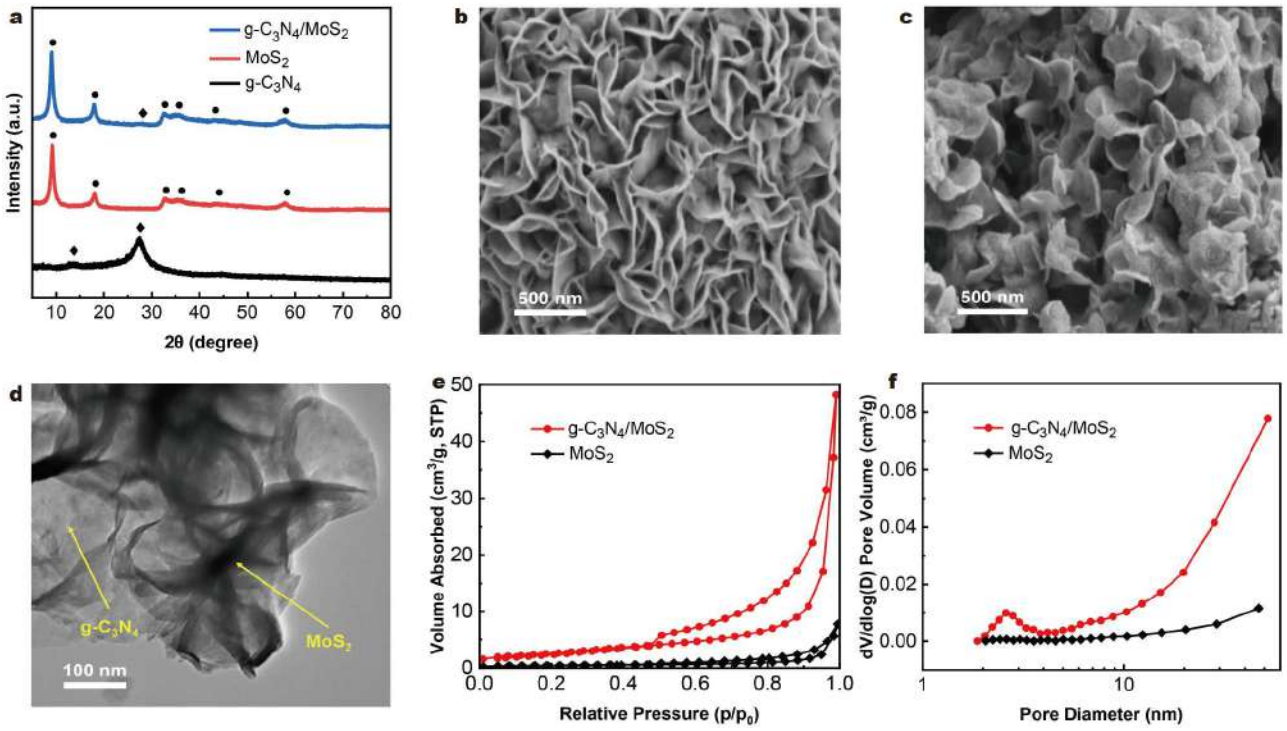

Figure 1 (a) XRD patterns of g-C_3N_4, MoS_2, and g-C_3N_4/MoS_2. SEM images of (b) MoS_2 and (c) g-C_3N_4/MoS_2. (d) TEM image of g-C_3N_4/MoS_2. (e) N_2 adsorption-desorption isotherms and (f) pore size distribution of MoS_2 and g-C_3N_4/MoS_2.

crystal plane [34]. Similarly, the weak peak at 13.4° corresponds to the interlayer stacking of the aromatic system, identified as the (100) crystal plane [30]. The red line corresponds to the spectrum of MoS_2, and the peak position indicated by the black dot can be analyzed using the reference figure (JCPDS 37-1492). Three prominent diffraction peaks are observed at 32.7°, 35.9°, and 58.4°, corresponding to the (100), (102), and (110) crystal planes of MoS_2, respectively [34]. In the low-angle region, two new diffraction peaks appeared at 9.1° and 18.2°. Notably, the interplanar spacing corresponding to the former is exactly twice that of the latter, suggesting the formation of a novel layered structure and the successful synthesis of the 2H-MoS_2 phase [35,36]. Fig. 1a also shows the XRD pattern of the g-C_3N_4/MoS_2 heterojunction sample, as indicated by the blue line (without specific instructions, the mass content of g-C_3N_4 was 150 mg). The peak value at 27.5° is consistent with g-C_3N_4, confirming that its crystal structure remains unchanged. However, a reduction in the diffraction peak intensity of g-C_3N_4 is observed. Additionally, the angular displacement of the diffraction peaks at 9.1° and 18.2° is diminished compared to that in pure 2H-MoS_2, indicating a possible interaction between MoS_2 and g-C_3N_4 [37].

The SEM images of MoS_2 and g-C_3N_4/MoS_2 are shown in Fig. 1b, c, respectively. MoS_2 exhibits a distinctive sheet-like morphology, characterized by vertically aligned nanosheets with uniform spacing and dimensions [38]. The SEM image of g-C_3N_4/MoS_2 reveals that the MoS_2 nanosheet structure remains intact following the addition of g-C_3N_4. The MoS_2 nanosheets are neatly arranged and tightly bound to the g-C_3N_4 component by the hydrothermal method. In contrast to the dense structure of MoS_2 sheets, the g-C_3N_4/MoS_2 material exhibits a loose sheet structure that is enveloped by the g-C_3N_4. This configuration can significantly enhance both the specific surface area and porosity [33]. Additionally, this robust adhesive structure fosters strong interfacial electron coupling, thereby enhancing dynamic charge transport under light irradiation [39].

To further explore the interfacial properties of the synthesized g-C_3N_4/MoS_2 heterojunction, TEM was conducted. As shown in Fig. 1d, the TEM data indicate that the MoS_2 nanosheets have been successfully modified by the g-C_3N_4, with both components exhibiting strong interfacial contact. A clear boundary differentiation between g-C_3N_4 and MoS_2 is evident, underscoring the well-defined interface within the heterojunction material [35]. From the above analysis, it can be concluded that we successfully synthesized the g-C_3N_4/MoS_2 heterojunction material. The intrinsic electric field generated by the heterojunction can facilitate the separation and transport of photogenerated carriers, thereby significantly enhancing the material's electrical conductivity [40]. The N_2 adsorption-desorption isotherms and pore size distribution of MoS_2 and g-C_3N_4/MoS_2 materials are shown in Fig. 1e, f. The BET specific surface area of the g-C_3N_4/MoS_2 heterojunction increases to 9.48 m^2/g, which is higher than that of MoS_2 (1.44 m^2/g). The pore size of g-C_3N_4/MoS_2 is slightly larger than that of MoS_2. The pores of the g-C_3N_4/MoS_2 composite primarily originate from the g-C_3N_4. During the synthesis of g-C_3N_4, the thermal decomposition of urea generates NH_3, H_2O, and CO_2. The release of these gases promotes the formation of the porous structure [41]. These results show that the heterojunction material possesses a greater specific surface area, which can provide more adsorption sites for zinc-ions [33].

The elemental composition and chemical states of carbon, nitrogen, molybdenum, sulfur, and oxygen in the g-C_3N_4/MoS_2 material were determined via XPS, as shown in Fig. 2a. The O 1s peak observed in Fig. 2a results from the unavoidable adsorption

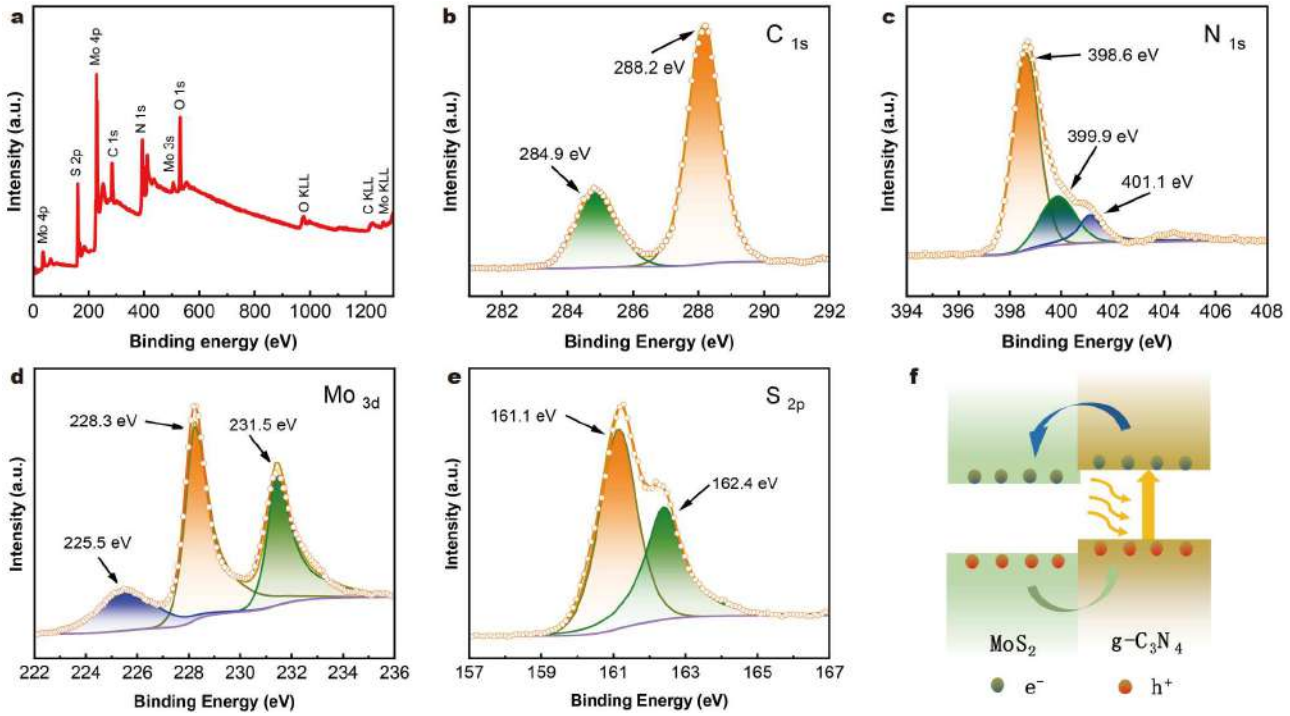

Figure 2 (a) XPS spectra of g-C_3N_4/MoS_2 materials, along with high-resolution XPS spectra for (b) C 1s, (c) N 1s, (d) Mo 3d, and (e) S 2p elements. (f) A diagram illustrating the flow direction of photogenerated carriers in the g-C_3N_4/MoS_2 heterojunction.

of environmental oxygen species, such as H_2O and O_2, on the surface of the g-C3N4/MoS_2 powder [42]. Furthermore, partial g-C_3N_4/MoS_2 materials may be slightly oxidized during the synthesis process [43]. According to the decomposition and fitting of the C 1s spectral peak, the peaks at 284.9 and 288.2 eV correspond to C–C/C=C bonds and N–C=N bonds, as illustrated in Fig. 2b [40]. Fig. 2c presents the spectra of the N 1s peak, which is deconvoluted into three distinct peaks at 398.6, 399.9, and 401.1 eV. These peaks can be attributed to the presence of sp^2-bonded N atoms, tertiary groups, and amino functional groups, respectively [44]. The two peaks observed at 228.3 eV (Mo $3d_{5/2}$) and 231.5 eV (Mo $3d_{3/2}$) in Fig. 2d exhibit a spin-energy separation of 3.2 eV, indicating that the Mo element within the g-C_3N_4/MoS_2 heterojunction predominantly exists in the Mo^{4+} state [45]. The blue peak at 225.5 eV in Fig. 2d is attributed to the S 2s orbital. The S 2s peak at 225.5 eV is very close to the Mo 3d peak at 228.3 eV and even overlaps with it. If the photoemission features of the S 2s are removed from the Mo 3d spectrum, the analysis of the Mo 3d signals will become inaccurate. This phenomenon is commonly observed in the XPS analysis of MoS_2 [37]. In Fig. 2e, the S 2p peaks at 161.1 and 162.4 eV can be assigned to S $2p_{3/2}$ and S $2p_{1/2}$, respectively. The S element in the heterojunction materials exists in the S^{2-} state, which further confirms the successful synthesis of MoS_2 within these materials [44].

The band position diagram of the g-C_3N_4/MoS_2 heterojunction material is presented in Fig. 2f [39]. To evaluate the photoactivity of heterojunction materials and determine the optimal quantity of g-C_3N_4, the variations in the photocurrent of g-C_3N_4, MoS_2, and g-C_3N_4/MoS_2 heterojunction materials are measured using a three-electrode system at 0 V bias voltage under illumination (the illumination source operates under the AM 1.5 G illumination standard unless otherwise specified). The light source is interrupted every 20 s. As shown in Fig. 3a, the photocurrent density of g-C_3N_4 and MoS_2 is lower than that of the g-C_3N_4/MoS_2 materials. This phenomenon is closely related to the heterojunction, which creates interfaces that promote carrier separation and transport. Under illumination, the well-matched band alignment between the g-C_3N_4 and the MoS_2 facilitates the transport of photogenerated electrons from the g-C_3N_4 to the MoS_2, while enabling the migration of photogenerated holes in the opposite direction, as illustrated in Fig. 2f. This directional charge migration effectively reduces the recombination probability of electron-hole pairs, thereby enhancing the utilization efficiency of photogenerated charges [46,47]. In addition, the heterojunctions can expand the light absorption range. The MoS_2 exhibits exceptional absorption in the visible light spectrum, while the g-C_3N_4 mainly absorbs the ultraviolet light. Thus, the g-C_3N_4/MoS_2 heterojunction achieves a broader light absorption range, improving the photocurrent responses [32]. Fig. 3a also shows the effect of the mass ratio between g-C_3N_4 and MoS_2 on the photocurrent. The heterojunction materials with 150 mg of the g-C_3N_4 show the strongest photoresponse, indicating the most effective photoactive configuration.

As depicted in Fig. S1, applying a bias voltage of 0.5 V to the three-electrode system featuring a g-C_3N_4/MoS_2 photoelectrode results in a corresponding increase in photocurrent of approximately 230 μA/cm^2. The photocurrent curve exhibits a characteristic wavy pattern corresponding to the switching of the light source. It has been demonstrated that illumination can effectively enhance the separation and transport of photogenerated carriers when a large bias voltage is applied [48,49]. Fig. 3b illustrates the CV responses of the g-C_3N_4/MoS_2 heterojunction electrode within a three-electrode system, compar-

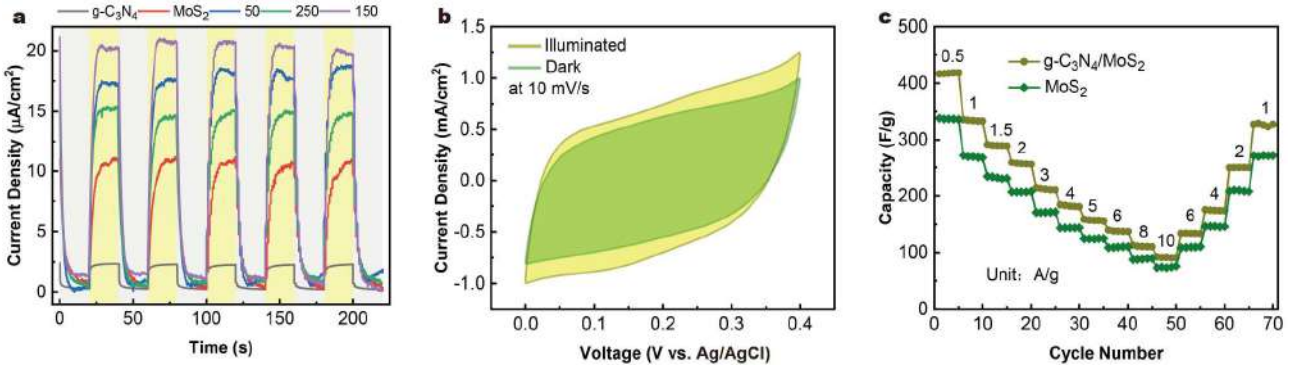

Figure 3 (a) Change in transient photocurrent response values for different materials. The black line represents g-C_3N_4, while the red line represents MoS_2. The blue, purple, and cyan lines correspond to g-C_3N_4/MoS_2 composites containing 50, 150, and 250 mg of g-C_3N_4, respectively. (b) CV at a scan rate of 10 mV/s under both light and dark conditions. (c) Rate capacity tests of PA-ZICs using MoS_2 and g-C_3N_4/MoS_2 electrode materials in the dark.

ing its performance in light and darkness. The specific capacity enhancement rate of the capacitor is calculated using Equation (1):

$$\eta=\frac{C_{\text{illumination}}-C_{\text{dark}}}{C_{\text{dark}}}\times 100\%. \quad (1)$$

The specific capacity of $C_{\text{illumination}}$ and C_{dark} under illumination and dark conditions was measured at the same scan rate [30]. Under illuminated conditions, the capacity increases by 25.42% during the cycle. Photogenerated holes exhibit a significant ability to absorb additional anions, resulting in an overall increase in capacitance [50,51].

Fig. S2 shows the structure diagram of the PA-ZIC. A 10 mm light transmission hole was created in the cathode shell to serve as a light intake window, using a coin capacitor (CR2032). The photocathode is fixed to the cathode shell of the capacitor, and the photo-assisted coin capacitor is assembled according to the standard procedures. Under dark conditions, the PA-ZIC cycle rate of g-C_3N_4/MoS_2 and MoS_2 electrode materials was tested, as illustrated in Fig. 3c. The rate performance of the g-C_3N_4/MoS_2 electrode material is significantly superior to that of the pure MoS_2 capacitor. At a current density of 1 A/g, the specific capacity of the MoS_2 material capacitor is measured at 269.69 F/g. In contrast, the specific capacity of the g-C_3N_4/MoS_2 capacitor significantly increases to 334.35 F/g, indicating a notable enhancement of 23.85%. This improvement can be attributed to the larger specific surface area of the g-C_3N_4/MoS_2 heterojunction compared to that of pure MoS_2, thereby providing more active sites for the adsorption of metal ions.

Under dark conditions, CV curves were tested at scan rates ranging from 5 to 100 mV/s, as shown in Fig. 4a. The CV curves of the zinc-ion capacitor do not exhibit any distinct peaks associated with faradaic redox reactions. Furthermore, the specific capacitance of the capacitor within the 0.2 to 1 V voltage window gradually decreases as the scanning rate increases [52,53]. We also tested the CV performance of the zinc-ion capacitor over 500 cycles at a scanning rate of 25 mV/s in the dark (Fig. 4b). The capacitance of the zinc-ion capacitor increases slightly during the first 100 cycles, reaching a value of 100.76%. This enhancement is attributed to the intermittent charge and discharge processes continuously improving the adsorption performance of the g-C_3N_4/MoS_2 electrode [30]. As the CV cycle progresses, there is a gradual decline in the storage capacity of a zinc-ion capacitor. After the 300th and 500th cycles, the capacitance retains 91.48% and 88.68% of its initial value, respectively. This indicates that the adsorption stability of zinc-ion capacitors is relatively robust [53].

To investigate the influence of light on the performance of zinc-ion capacitors, we compared the CV performance of these capacitors under both dark and illuminated conditions. Fig. 4c–f show CV curves at scan rates of 5, 10, 50, and 100 mV/s [54]. Under illuminated conditions, the current density of the zinc-ion capacitors exhibited varying increases, resulting in enhancements in the CV area of 39.1%, 30.6%, 25.04%, and 18.72%, respectively. This indicates a significant increase in the capacitance of the capacitor. Notably, the lower the scan rate, the higher the capacitance. The capacitor absorbs more solar energy, and the photogenerated carriers contribute to enhancing the capacitor's energy storage performance [53,55,56]. However, we noticed a notable decrease in the specific capacitance difference between the illuminated and dark conditions. This phenomenon arises from the large input current at the high scan rates, which induces concentration polarization at the electrode/electrolyte interface. Thus, the photogenerated electrons are unable to adsorb additional Zn^{2+} ions [24]. Furthermore, the photoelectrode does not have enough time to generate more electron-hole pairs, which reduces the effectiveness of light in enhancing performance [57]. There is no apparent pseudocapacitance behavior observed in CV images, and illumination cannot change the structural properties of the capacitors. To eliminate the thermal effects, cooling measures are required to maintain a constant temperature for the capacitor under illumination [56]. We employed air-cooling to control the temperature fluctuations of the capacitor. This method provides real-time feedback on the cooling result by measuring the surface temperature of the PA-ZIC. It was found that the surface temperature of the PA-ZIC was the same as that of other coin-type capacitors.

We evaluated the rate capability of the zinc-ion capacitor at current densities ranging from 1 to 10 A/g under both dark and illuminated conditions. This assessment aimed to investigate the influence of illumination on the electrochemical performance of zinc-ion capacitors. As depicted in Fig. 5a, the capacitance of the two capacitors remains nearly identical at 0.5 A/g under dark conditions. However, as the current density increases from 1 to 10 A/g, the discharge capacity of the capacitor under illuminated conditions significantly surpasses that in the dark. The specific

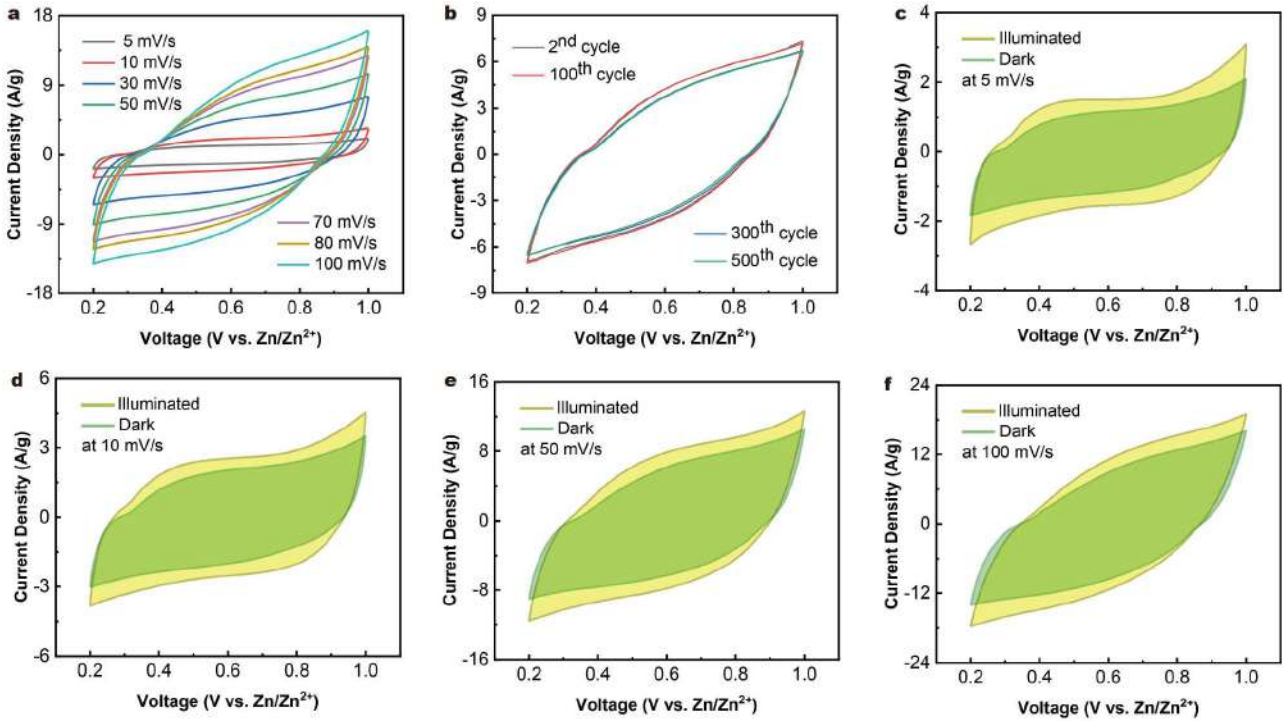

Figure 4 (a) CV of a PA-ZIC in a 3 M $Zn(CF_3SO_3)_2$ aqueous electrolyte (5–100 mV/s) in darkness. (b) CV of the PA-ZIC at a scan rate of 25 mV/s during the 2nd (black), 100th (red), 300th (blue), and 500th (cyan) cycles in darkness. CV of the PA-ZIC at scan rates of (c) 5, (d) 10, (e) 50, and (f) 100 mV/s under both illuminated and dark conditions.

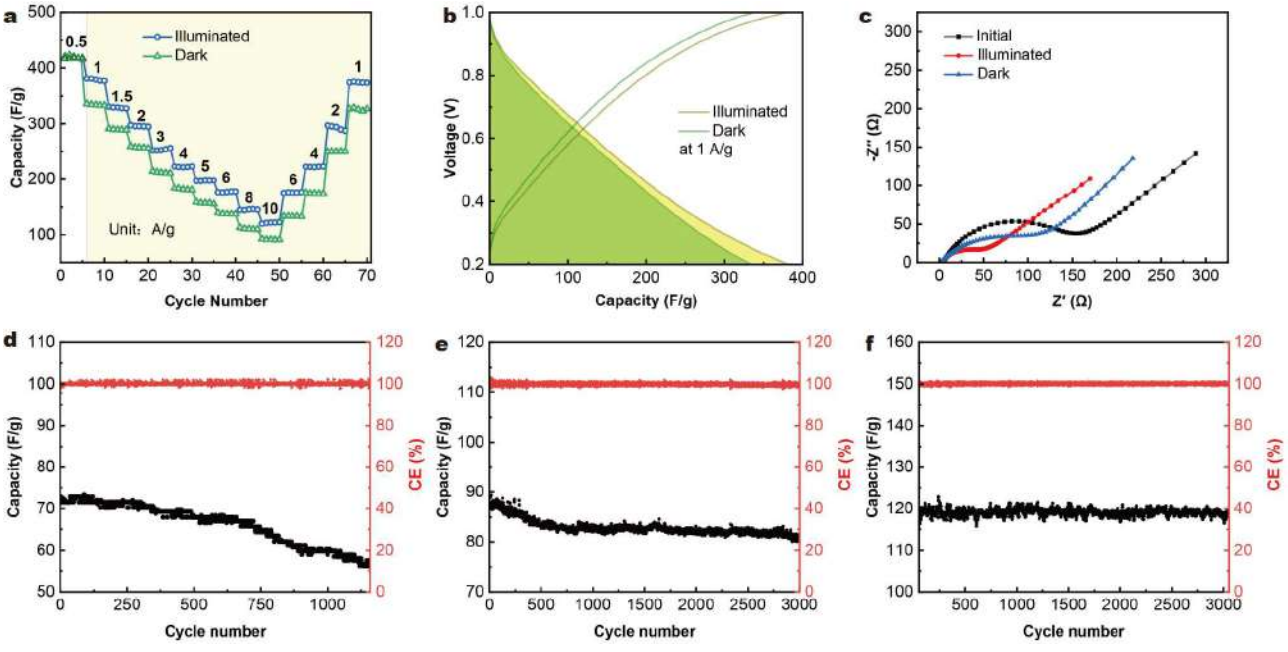

Figure 5 (a) Rate capacity tests of the PA-ZIC under illuminated and dark conditions. The green triangular symbols and blue circular symbols represent the specific discharge capacity of the PA-ZIC under dark and illuminated conditions, respectively. (b) GCD tests were conducted at a specific current density of 1 A/g. (c) EIS of PA-ZICs. The impedance response after charging and discharging was compared under initial, dark, and illuminated conditions. (d) GCD performance of a MoS_2 electrode PA-ZIC under dark conditions. GCD performance of g-C_3N_4/MoS_2 electrode PA-ZICs (e) under dark conditions and (f) under illumination conditions. All GCD tests were conducted at a current density of 10 A/g.

capacitance calculation Equation (2) is expressed as follows:

$$C = \frac{It}{\Delta V m}, \quad (2)$$

where C represents the specific capacitance of the capacitor (F/g), m is the mass of the photoelectrode (g), I is the current (A), ΔV is the voltage window (V), and t is the discharge time (s)

[33]. From Fig. 5b, it is evident that at a current density of 1 A/g, the specific capacitance increases from 334.35 to 380.93 F/g, representing a rise of 13.93%.

According to the experimental phenomena and analysis results mentioned above, the photo-assisted effect can enhance the energy storage performance of zinc-ion capacitors. During the photo-assisted discharge process, the g-C_3N_4/MoS_2 heterojunction generates electron-hole pairs. When the electrons are excited by light and the electrons in the external circuit co-adsorb Zn^{2+} ions from the electrolyte, it enhances the adsorption effect of the capacitor photocathode [50,58]. During the photo-assisted charging process, the photo-generated holes facilitate the complete desorption of Zn^{2+} ions from the photocathode. The photogenerated electrons, along with those from the external circuit, are transferred to the anode, thereby increasing capacitance [59]. Under illuminated conditions, the electron-hole pairs generated by the g-C_3N_4/MoS_2 photoelectrode actively participate in the energy storage process of the capacitor, enhancing its electrochemical performance.

We also conducted the EIS of zinc-ion capacitors after rate capacity measurement, as shown in Fig. 5c. Before the rate capacity test, the initial charge transfer resistance of the capacitor is 129.2 Ω (R_{ct}) and the ohmic resistance is 4.5 Ω (R_s). In dark conditions, the R_{ct} and R_s values become 110.5 and 1.71 Ω after the rate capacity tests. Under illuminated conditions, the capacitor's transfer resistance decreases further to 36.26 Ω, indicating a significant reduction in the capacitor. These phenomena demonstrate that the presence of photogenerated carriers enhances the conductivity of the electrode sheet and decreases the charge transfer resistance of the capacitor [60]. The stability of zinc-ion capacitors during GCD also serves as a significant index to evaluate electrochemical properties. To assess this, we initially tested the GCD performance of the zinc-ion capacitor with a MoS_2 electrode in the dark, as illustrated in Fig. 5d. After 1160 cycles, the specific capacity of the capacitor decreased by 21.9% at a current density of 10 A/g. We also cycled the PA-ZIC with a g-C_3N_4/MoS_2 electrode for 3000 cycles in the dark (as shown in Fig. 5e). The results indicate that the specific capacity of the capacitor decreases by 5.64% during the first 600 cycles. After 3000 cycles, the capacity retention rate stabilizes at 91.8%. Fig. 5f illustrates the performance of the PA-ZIC from the 50th to the 3050th cycle under illuminated conditions. Slight fluctuations in capacitor capacity are observed throughout the operating cycles, which may be attributed to variations in the brightness of the light source. Nevertheless, there is almost no attenuation of the coulomb efficiency, and the capacity retention ratio remains above 99% after cycling. Compared to other capacitors, the photo-assisted capacitor offers a significant advantage (Table S1). Fig. S3 shows the mechanism of the photo-enhanced cycling stability. The stable cycling performance can be attributed to their superior conductivity under illumination, as depicted in Fig. 5c [61,62]. The built-in electric field within the g-C_3N_4/MoS_2 electrode promotes the separation and transport of the photogenerated electron-hole pairs, increasing the concentration of free electrons, which further enhances the conductivity of the material [23]. Additionally, the high conductivity of the photoelectrode is also improved by the increased light absorption resulting from the material's large surface area [63]. As a result, the PA-ZIC featuring the g-C_3N_4 /MoS_2 photoanode exhibits excellent electrochemical performance.

CONCLUSIONS

This work proposes the use of g-C_3N_4/MoS_2 dual-functional materials for the assembly of photo-assisted zinc-ion capacitors. SEM and BET characterization confirm that g-C_3N_4 modified MoS_2 leads to an increased specific surface area. When the capacitor is exposed to light, the g-C_3N_4/MoS_2 photoelectrode generates charge carriers under the influence of the intrinsic electric field, thereby enhancing the separation and transport of the carriers. Compared to dark conditions, the photo-assisted effect improves the adsorption and desorption processes of zinc ions, significantly increasing the specific capacity of the zinc-ion capacitors. The continuous generation of electron-hole pairs by the g-C_3N_4/MoS_2 photoelectrode under illumination reduces the resistance of the capacitor. This phenomenon contributes to the exceptional cycle stability demonstrated by the photo-assisted zinc-ion capacitor. This paper introduces an advanced methodology designed to improve the specific capacity and cycle longevity of zinc-ion capacitors.

Received 2 November 2024; accepted 31 December 2024; published online 8 February 2025

1 Dong X, Chen X, Jiang X, *et al.* Light-assisted energy storage devices: principles, performance, and perspectives. Adv Energy Mater, 2023, 13: 2301143
2 Yang M, Wang D, Ling Y, *et al.* Emerging advanced photo-rechargeable batteries. Adv Funct Mater, 2024, 34: 2410398
3 Tichter T, Naumann K, Vesborg PCK. Photoelectrochemical, all-soluble iron redox-flow battery for the direct conversion of solar energy. Electrochim Acta, 2024, 487: 144140
4 Chen P, Li TT, Li GR, *et al.* Quasi-solid-state solar rechargeable capacitors based on *in-situ* Janus modified electrode for solar energy multiplication effect. Sci China Mater, 2020, 63: 1693–1702
5 Wang K, Li H, Xu Z, *et al.* Emerging photo-integrated rechargeable aqueous zinc-ion batteries and capacitors toward direct solar energy conversion and storage. Carbon Neutralization, 2023, 2: 37–53
6 Prakash HC, Kumar MS, Lin TW, *et al.* Photo-assisted capacitive performance of V_2O_5 supercapacitor. Electrochim Acta, 2023, 469: 143229
7 Sun H, Xiang X, Wang X, *et al.* Advanced photo-rechargeable lithium- and zinc-ion batteries: progress and prospect. J Power Sources, 2024, 598: 234204
8 Bao W, Shen H, Wang R, *et al.* Photo-assisted rechargeable batteries: principles, performance, and development. J Mater Chem A, 2023, 11: 18605–18625
9 Wang W, Zhang X, Lin J, *et al.* A photoresponsive battery based on a redox-coupled covalent-organic-framework hybrid photoelectrochemical cathode. Angew Chem Int Ed, 2022, 61: e202214816
10 Zhang X, Song WL, Wang M, *et al.* Photo-electrochemical enhanced mechanism enables a fast-charging and high-energy aqueous Al/MnO_2 battery. Energy Storage Mater, 2022, 45: 586–594
11 Wang J, Wang Y, Zhu C, *et al.* Photoinduced rechargeable lithium-ion battery. ACS Appl Mater Interfaces, 2022, 14: 4071–4078
12 Zhu T, He Z, An Z, *et al.* Enhancing solar energy harvest by Cu_2S/CuCl heteroarrays with enriched sulfur vacancies for photo-rechargeable pseudocapacitors. Sci China Mater, 2023, 66: 2216–2226
13 Jiao L, Zhang X, Feng Y, *et al.* Coupled solar battery with 6.9 % efficiency. Angew Chem Int Ed, 2023, 62: e202306506
14 Momeni MM, Navandian S, Aydisheh HM, *et al.* Photo-assisted rechargeable supercapacitors based on nickel-cobalt-deposited tungsten-doped titania photoelectrodes: a novel self-powered supercapacitor. J Power Sources, 2023, 557: 232588
15 Ramalingam K, Wei Q, Babu G, *et al.* Photo-assisted rechargeable battery desalination. ACS Appl Mater Interfaces, 2022, 14: 30907–30913
16 Liu X, Yuan Y, Liu J, *et al.* Utilizing solar energy to improve the oxygen evolution reaction kinetics in zinc–air battery. Nat Commun, 2019, 10:

4767
17 Liang S, Zheng LJ, Song LN, *et al.* Accelerated confined mass transfer of MoS_2 1D nanotube in photo-assisted metal-air batteries. Adv Mater, 2024, 36: 2307790
18 Si J, Guo C, Liu H, *et al.* Photo-induced self-catalysis of nano-Bi_2MoO_6 for solar energy harvesting and charge storage. RSC Adv, 2020, 10: 38033–38037
19 Ansari RM, Chamola S, Ahmad S. Ruddlesden-Popper 2D perovskite-MoS_2 hybrid heterojunction photocathodes for efficient and scalable photo-rechargeable Li-ion batteries. Small, 2024, n/a: 2401350
20 Tang Z, Dai J, Wei W, *et al. In situ* generation of ultrathin MoS_2 nanosheets in carbon matrix for high energy density photo-responsive supercapacitors. Adv Sci, 2022, 9: 2201685
21 Cao M, Wang D, Feng Y, *et al.* Design of a light-sensitive tubular MoS_2/C composite as the cathode for photo-enhanced rechargeable zinc-ion batteries. J Mater Chem A, 2024, 12: 5924–5930
22 Kumar A, Thakur P, Sharma R, *et al.* Photo rechargeable Li-ion batteries using nanorod heterostructure electrodes. Small, 2021, 17: 2105029
23 Li J, Zhang Y, Mao Y, *et al.* Dual-functional Z-scheme TiO_2@MoS_2@NC multi-heterostructures for photo-driving ultrafast sodium ion storage. Angew Chem Int Ed, 2023, 62: e202303056
24 Wen X, Zhong Y, Chen S, *et al.* 3D hierarchical sunflower-shaped MoS_2/SnO_2 photocathodes for photo-rechargeable zinc ion batteries. Adv Sci, 2024, 11: 2309555
25 Li J, Liu E, Ma Y, *et al.* Synthesis of MoS_2/g-C_3N_4 nanosheets as 2D heterojunction photocatalysts with enhanced visible light activity. Appl Surf Sci, 2016, 364: 694–702
26 Chenrayan S, S. Chandra K, Manickam S. Ultrathin MoS_2 sheets supported on N-rich carbon nitride nanospheres with enhanced lithium storage properties. Appl Surf Sci, 2017, 410: 215–224
27 Boruah BD, Wen B, De Volder M. Molybdenum disulfide-zinc oxide photocathodes for photo-rechargeable zinc-ion batteries. ACS Nano, 2021, 15: 16616–16624
28 Du XY, Song LN, Liang S, *et al.* Photo-assisted chemical self-rechargeable zinc ion batteries with high charging and discharging efficiency. Angew Chem Int Ed, 2024, 63: e202411845
29 Hu T, Lian W, Hu K, *et al.* Photo-energized MoS_2/CNT cathode for high-performance Li–CO_2 batteries in a wide-temperature range. Nano-Micro Lett, 2024, 17: 5
30 Boruah BD, Mathieson A, Wen B, *et al.* Photo-rechargeable zinc-ion capacitor using 2D graphitic carbon nitride. Nano Lett, 2020, 20: 5967–5974
31 Gouder A, Podjaski F, Jiménez-Solano A, *et al.* An integrated solar battery based on a charge storing 2D carbon nitride. Energy Environ Sci, 2023, 16: 1520–1530
32 Zhang X, Tian F, Lan X, *et al.* Building P-doped MoS_2/g-C_3N_4 layered heterojunction with a dual-internal electric field for efficient photocatalytic sterilization. Chem Eng J, 2022, 429: 132588
33 Tian S, Zhang X, Zhang Z. Capacitive deionization with MoS_2/g-C_3N_4 electrodes. Desalination, 2020, 479: 114348
34 Majumder S, Shao M, Deng Y, *et al.* Ultrathin sheets of MoS_2/g-C_3N_4 composite as a good hosting material of sulfur for lithium–sulfur batteries. J Power Sources, 2019, 431: 93–104
35 Xie J, Zhang J, Li S, *et al.* Controllable disorder engineering in oxygen-incorporated MoS_2 ultrathin nanosheets for efficient hydrogen evolution. J Am Chem Soc, 2013, 135: 17881–17888
36 Yan H, Chu L, Li Z, *et al.* 2H-MoS_2/$Ti_3C_2T_x$ MXene composites for enhanced NO_2 gas sensing properties at room temperature. Sens Actuat Rep, 2022, 4: 100103
37 Fageria P, Sudharshan KY, Nazir R, *et al.* Decoration of MoS_2 on g-C_3N_4 surface for efficient hydrogen evolution reaction. Electrochim Acta, 2017, 258: 1273–1283
38 Chen Y, Su F, Xie H, *et al.* One-step construction of S-scheme heterojunctions of N-doped MoS_2 and S-doped g-C_3N_4 for enhanced photocatalytic hydrogen evolution. Chem Eng J, 2021, 404: 126498
39 Zhu K, Luan X, Matras-Postolek K, *et al.* 2D/2D MoS_2/g-C_3N_4 layered heterojunctions with enhanced interfacial electron coupling effect. J Electroanal Chem, 2021, 893: 115350
40 Liu Y, Xu X, Zhang J, *et al.* Flower-like MoS_2 on graphitic carbon nitride for enhanced photocatalytic and electrochemical hydrogen evolutions. Appl Catal B-Environ, 2018, 239: 334–344
41 Zhang M, Xu J, Zong R, *et al.* Enhancement of visible light photocatalytic activities via porous structure of g-C_3N_4. Appl Catal B-Environ, 2014, 147: 229–235
42 Hou J, Xu J, Hao X, *et al.* Photoelectric antifouling performance of molybdenum disulfide/graphite carbon nitride/polyaniline coatings under visible light. Appl Surf Sci, 2024, 657: 159794
43 Liu J, Dong Y, Zhang Y, *et al.* Enhanced synergistic performance of g-C_3N_4/MoS_2 with hollow structure for tetracycline photocatalytic degradation in complex environments: performance and mechanism. J Cleaner Production, 2024, 451: 141983
44 Sima L, Li D, Dong L, *et al.* Facile preparation of porous g-C_3N_4/MoS_2 heterojunction for hydrogen production under simulated sunlight. Mater Today Sustainability, 2022, 20: 100217
45 Lei D, Shang W, Zhang X, *et al.* Facile synthesis of heterostructured MoS_2–MoO_3 nanosheets with active electrocatalytic sites for high-performance lithium–sulfur batteries. ACS Nano, 2021, 15: 20478–20488
46 Sun X, Tiwari D, Fermin DJ. Nanostructured $LaFeO_3$ photocathodes with onset potentials for the hydrogen evolution reaction over 1.4 V vs. RHE. J Electrochem Soc, 2019, 166: H764–H768
47 Lv Y, Sun X, Mi C, *et al.* A photo rechargeable capacitor based on the p–n heterojunction of ZnO/ZIF-67 showing enhanced photovoltage. APL Mater, 2024, 12: 081113
48 Sun X, Wang M, Li HF, *et al.* Pristine $GaFeO_3$ photoanodes with surface charge transfer efficiency of almost unity at 1.23 V for photoelectrochemical water splitting. Adv Sci, 2023, 10: 2205907
49 Sun X, Tiwari D, Li M, *et al.* Decoupling the impact of bulk and surface point defects on the photoelectrochemical properties of $LaFeO_3$ thin films. Chem Sci, 2022, 13: 11252–11259
50 Yang W, Wang J, Gao S, *et al.* Photo-assisted charging of carbon fiber paper-supported CeO_2/MnO_2 heterojunction and its long-lasting capacitance enhancement in dark. J Adv Ceram, 2022, 11: 1735–1750
51 Renani AS, Momeni MM, Aydisheh HM, *et al.* New photoelectrodes based on bismuth vanadate-V_2O_5@TiNT for photo-rechargeable supercapacitors. J Energy Storage, 2023, 62: 106866
52 Mohsen Momeni M, Mohammadzadeh Aydisheh H, Lee BK. Effectiveness of MnO_2 and V_2O_5 deposition on light fostered supercapacitor performance of $WTiO_2$ nanotube: novel electrodes for photo-assisted supercapacitors. Chem Eng J, 2022, 450: 137941
53 Boruah BD, Wen B, Nagane S, *et al.* Photo-rechargeable zinc-ion capacitors using V_2O_5-activated carbon electrodes. ACS Energy Lett, 2020, 5: 3132–3139
54 Deka Boruah B, Mathieson A, Park SK, *et al.* Vanadium dioxide cathodes for high-rate photo-rechargeable zinc-ion batteries. Adv Energy Mater, 2021, 11: 2100115
55 Liu X, Andersen H, Lu Y, *et al.* Porous carbon coated on cadmium sulfide-decorated zinc oxide nanorod photocathodes for photo-accelerated zinc ion capacitors. ACS Appl Mater Interfaces, 2023, 15: 6963–6969
56 Dong Q, Wei M, Zhang Q, *et al.* Photoassisted Li-ion de-intercalation and $Ni^{\delta+}$ valence conversion win-win boost energy storage performance in Ni/CdS@Ni_3S_2-based Li-ion battery. Chem Eng J, 2023, 459: 141542
57 Azadmanjiri J, Regner J, Sturala J, *et al.* Decoding niobium carbide MXene dual-functional photoactive cathode in photoenhanced hybrid zinc-ion capacitor. ACS Mater Lett, 2024, 6: 1338–1346
58 Xu C, Zhang X, Duan L, *et al.* A photo-assisted rechargeable battery: synergy, compatibility, and stability of a TiO_2/dye/Cu_2S bifunctional composite electrode. Nanoscale, 2020, 12: 530–537
59 Li J, Liu H, Sun K, *et al.* Dual-functional iodine photoelectrode enabling high performance photo-assisted rechargeable lithium iodine batteries. J Mater Chem A, 2022, 10: 7326–7332
60 Wang XX, Guan DH, Miao CL, *et al.* Metal–organic framework-based mixed conductors achieve highly stable photo-assisted solid-state lithium–oxygen batteries. J Am Chem Soc, 2023, 145: 5718–5729
61 Liu T, Li Y. Addressing the Achilles' heel of pseudocapacitive materials: long-term stability. InfoMat, 2020, 2: 807–842

62 Xing Z, Xu G, Han J, *et al.* Facing the capacity fading of vanadium-based zinc-ion batteries. Trends Chem, 2023, 5: 380–392
63 Wang Y, Du P, Pan H, *et al.* Increasing solar absorption of atomically thin 2D carbon nitride sheets for enhanced visible-light photocatalysis. Adv Mater, 2019, 31: 1807540

Acknowledgement This work was supported partially by the National Natural Science Foundation of China (52302250 and 52272200), the Hebei Natural Science Foundation (B2024502013), the State Key Laboratory of Alternate Electrical Power System with Renewable Energy Sources (LAPS21004 and LAPS202114), the Beijing Natural Science Foundation (2222076), the 2022 Strategic Research Key Project of Science and Technology Commission of the Ministry of Education, the China Postdoctoral Science Foundation (2022M721129), the Fundamental Research Funds for the Central Universities (2022MS030 and 2021MS028), and the NCEPU "Double First-Class" Program.

Author contributions Mi C designed and engineered the samples; Lv Y and Lv X conceived the post-fabrication tuning of random modes; Mi C and Yin X performed the experiments; Mi C and Yang J wrote the paper with support from Sun X. Sun X and Li M revised the manuscript and provided academic comments. All authors contributed to the general discussion.

Conflict of interest The authors declare that they have no conflict of interest.

Supplementary information Supplementary materials are available in the online version of the paper.

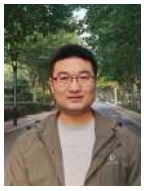

Changhua Mi is currently a doctoral student at the School of New Energy, North China Electric Power University. His research focuses on new types of storage devices, particularly those with photo-rechargeable capabilities.

Meicheng Li is a professor at North China Electric Power University and serves as the Dean of the School of New Energy. His primary focus is on the design and research of photo-rechargeable devices. Additionally, he is interested in the research and development of new energy technologies, such as perovskite solar cells and lithium-ion batteries.

用于光辅助增强锌离子电容器稳定性的g-C_3N_4修饰MOS_2光电极

米倡华, 孙鑫, 殷小净, 杨佳豪, 吕延龙, 吕小军, 李美成*

摘要 光辅助充电电容器是一种有吸引力的太阳能转换和储存装置, 但光电极的性能限制了它们的效果. 在这项工作中, g-C_3N_4修饰的MoS_2光电极表现出增强的光可充电性能. 结果表明, g-C_3N_4的引入增加了MoS_2光电极的表面积, 促进了载流子的输运, 从而提高了电容器的比容量和循环稳定性. 在AM 1.5 G照明下, 采用g-C_3N_4/MoS_2光电极制备的锌离子电容器在1 A/g下的比容量为380.93 F/g. 值得注意的是, 在10 A/g下循环3000次后, 光辅助锌离子电容器的容量保持在99%以上.